

Low-Power Phase Transition of Chalcogenide Glass Using Au Nanoparticle Plasmon Resonance

Tun Cao,* Kuan Liu, Li Lu, Jianxun Liu, Yan Jun Liu,* Kai Rong Qin, Hsiang Chen Chui, and Robert E. Simpson

Chalcogenide materials are attractive for all-photonic phase-change memories owing to their large optical contrast between amorphous and crystalline structural phases. However, high-power heating pulses are required to switch these structural phases, which can limit the cyclability. To reduce power, Au nanoparticles (NPs) are embedded in a typical chalcogenide phase-change material, $\text{Ge}_2\text{Sb}_2\text{Te}_5$ (GST). Raman analysis shows that a GST film crystallizes at a low optical power of 2 mW, which is almost 10 times lower than that of materials not embedded with NPs. This lower power is owing to the enhanced light absorbance through the strongly localized surface plasmon resonance (LSPR) of the Au NPs. The Au NPs embedded in the GST film scatter light at $\lambda = 587$ nm, which is close to Au NP's LSPR of ≈ 535 nm. Laser light at 532 nm is used to measure Raman scattering from the Au–GST system. The Raman scattering is enhanced by a factor 12 compared with a bare GST film. This study indicates that the GST film–Au NP system is suitable for high-speed, low-power, phase-change memory and for a new type of tunable surface-enhanced Raman scattering substrate.

1. Introduction

Chalcogenide phase-change random access thin films are of technological importance because they can rapidly and reversibly switch between amorphous and crystalline phases upon heating.^[1–3] Chalcogenide alloys are materials that are formed from sulfur, selenium, and tellurium. They can be produced in phase-change random access memory (PRAM) devices. For example, $\text{Ge}_2\text{Sb}_2\text{Te}_5$ (GST)-based PRAM has been used in commercial mobile electronics,^[4,5] and related materials are

currently used in Intel Optane Memory.^[6] GST is attractive for these applications because it can be reliably switched between amorphous and crystalline states millions of times, scaled to only 1.4 nm, and still retains phase transitions.^[7] Furthermore, it is compatible with complementary metal-oxide-semiconductor (CMOS) technology.^[8–11] To crystallize GST (Set operation), a material must be heated to above its crystallization temperature ($T_C = 483$ K) but below its melting temperature ($T_M = 873$ K).^[12–14] On the contrary, to reamorphize GST (Reset operation) from the crystalline state, an optical or electrical heating pulse of short duration and high power is required.^[15–17] This high-power requirement is a factor limiting a phase change material (PCM) application in tunable and reprogrammable photonics.

To overcome the limitations of GST, extensive investigations have been conducted to develop devices employing advanced nanostructures, low-conductivity encapsulating materials, and new chalcogenide alloys. For example, adding a metallic mirror reflects light back into the GST film, thereby reducing the crystallization power to 3.36 mW.^[18] Recently, perfect metamaterial absorbers have been introduced to enable an ultrafast crystallization of GST films under a low light intensity.^[19–21] All the schemes discussed above inevitably increase the design complexity of the devices, which consequently render fabrication more challenging and expensive. This motivates us to investigate low-cost and straightforward approaches to reduce the switching power of GST.

The coupling localized surface-plasmon resonances (LSPRs) in metallic nanoparticles (NPs) to layers has recently attracted considerable interest.^[22,23] An electric field can resonate strongly in the gap between the NPs and the film. The concomitant electromagnetic (EM) field enhancement of such an LSPR can be considerably larger than that of an individual NP resonator. We claim that these coupled LSPR resonances may fulfill the increasing need for chip-scale tunable photonic devices with low energy consumption.^[24–26]

Metallic NPs deposited on a film can enhance LSPR-based imaging^[27] and sensing,^[28] as well as benefit plasmon-mediated sensing applications, such as the surface-enhanced Raman scattering (SERS) of molecules^[29–34] and detection of local chemical reactions.^[35] Notably, metallic NPs can transport a therapeutic dose of heat under low exposures of extracorporeally applied

Prof. T. Cao, K. Liu, Prof. H. C. Chui, Prof. K. R. Qin
School of Optoelectronic Engineering and Instrumentation Science
Dalian University of Technology
Dalian 116024, China
E-mail: caotun1806@dlut.edu.cn

L. Lu, Prof. R. E. Simpson
Singapore University of Technology and Design
Singapore 487372, Singapore

Dr. J. Liu, Prof. Y. J. Liu
Department of Electrical and Electronic Engineering
Southern University of Science and Technology
Shenzhen 518055, China
E-mail: yjliu@sustech.edu.cn

 The ORCID identification number(s) for the author(s) of this article can be found under <https://doi.org/10.1002/adom.201901570>.

DOI: 10.1002/adom.201901570

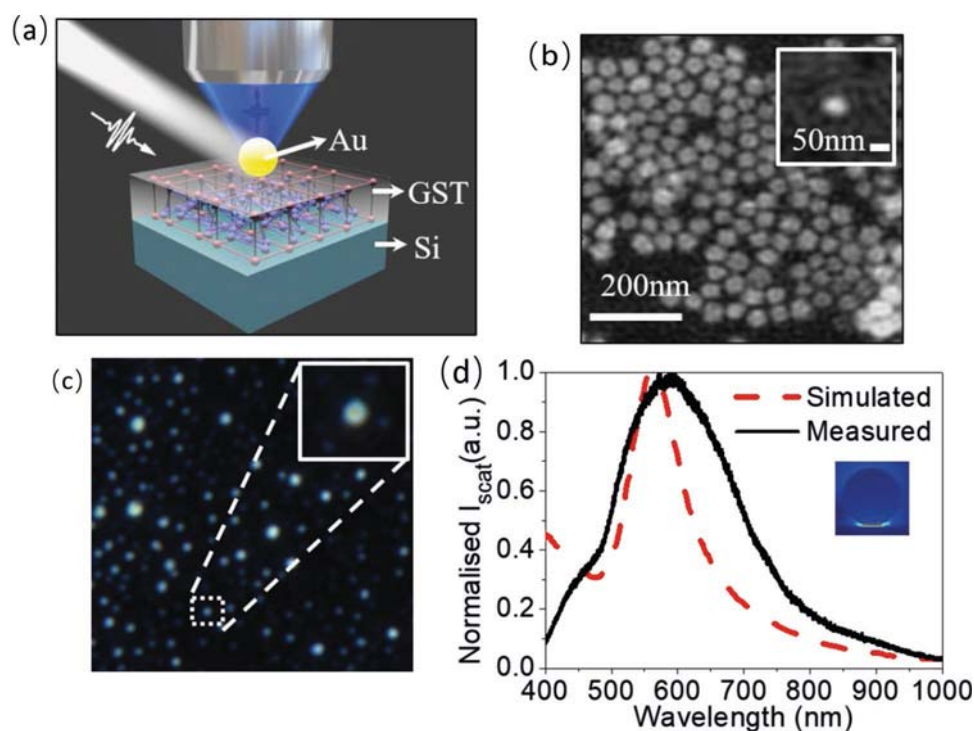


Figure 1. a) Optical setup for the scattering spectrum and dark-field measurement of individual Au NPs deposited on a GST thin film. b) Electron-beam lithography (EBL) image of the Au NPs. c) Dark-field microscopy image of 25 nm radius Au NPs on the GST film. d) Measured and calculated normalized I_{scat} spectra of the Au NPs coupled to the GST film. The solid black line shows the measured I_{scat} spectrum, and the dashed red line shows the simulated spectrum. The inset shows the simulated total E -field distribution at $\lambda = 563$ nm, where the structure was illuminated by white light with an incident angle of 70° , corresponding to the illumination angle of the dark-field experiment.

light in the near-infrared (NIR) spectrum. This may be applicable to photothermal therapy-based cancer treatment.^[36–38] Therefore, a question arises: can a similar mechanism increase the photothermal heating efficiency of PCMs? Coupling plasmon resonances to a film increases the reproducibility of the optical response, increases the structural stability of NPs, and provides a cost-effective and easy fabrication method.^[39,40] These features render the coupling thin films to NPs a promising method for low-power LSPR-enhanced switching in GST films.

In this study, the strong LSPR of Au NPs was used to enhance the photoheating of 35 nm thick GST films. Crystallized GST can be achieved with a low light power of 2 mW focused into a spot diameter of 1 μm . By this approach, a power reduction of at least 85% was achieved on the Au-NP-deposited GST film when compared with a monolithic bare GST film of equal size. Furthermore, we discovered that the Raman signal from GST was enhanced by a factor of 12 in comparison with a planar GST film. This amplification was caused by the enhanced electrical (E -) field in the gap between the GST film and the Au NPs, which is typically known as gap plasmons.^[41–44] Therefore, the proposed structure may act as a tunable SERS substrate for detecting trace amounts of analytes.

2. Results and Discussions

A 35 nm thick GST film was deposited onto a silicon substrate by sputtering. To generate a structure that supports LSPR, a

cluster of Au NPs was deposited from a colloidal solution onto the GST film, as detailed in Methods. This resulted in a well-defined LSPR signature in the visible spectral region. **Figure 1a** shows a schematic of the experimental setup for measuring the scattering spectra using dark-field microscopy. **Figure 1b** shows an electron-beam lithography (ELS-7500EX) image of the Au NPs sparsely distributed on the GST film. As shown in the SEM image, the Au NPs deposited onto the GST film have a similar radius of 25 ± 1 nm.

To achieve a dark-field image and a normalized scattering spectrum (I_{scat}) from individual Au NPs, we obliquely illuminated the structure with white light from a halogen bulb under the dark-field configuration. **Figure 1c** shows the dark-field microscope image of the Au NPs dispersed on the as-deposited amorphous GST film. The Au NPs on the GST layer appeared to be ring-shaped and scattered cyan light. It is noteworthy that all the Au NPs exhibited a comparable scattering intensity and color, indicating that they support similar plasmon modes. We measured the spectra from the NPs indicated by the dashed white square in **Figure 1c**. The corresponding normalized spectrum, I_{scat} of the individual Au NPs is presented by the solid black line in **Figure 1d**. The measured I_{scat} has a broad spectrum with a central peak at approximately $\lambda = 587$ nm. To determine the LSPR modes responsible for the features in the measured I_{scat} spectrum, numerical simulation was performed using the finite-difference time-domain (FDTD) method to solve Maxwell's equation. This simulated spectra qualitatively reproduced the measured scattering spectra and peaks at

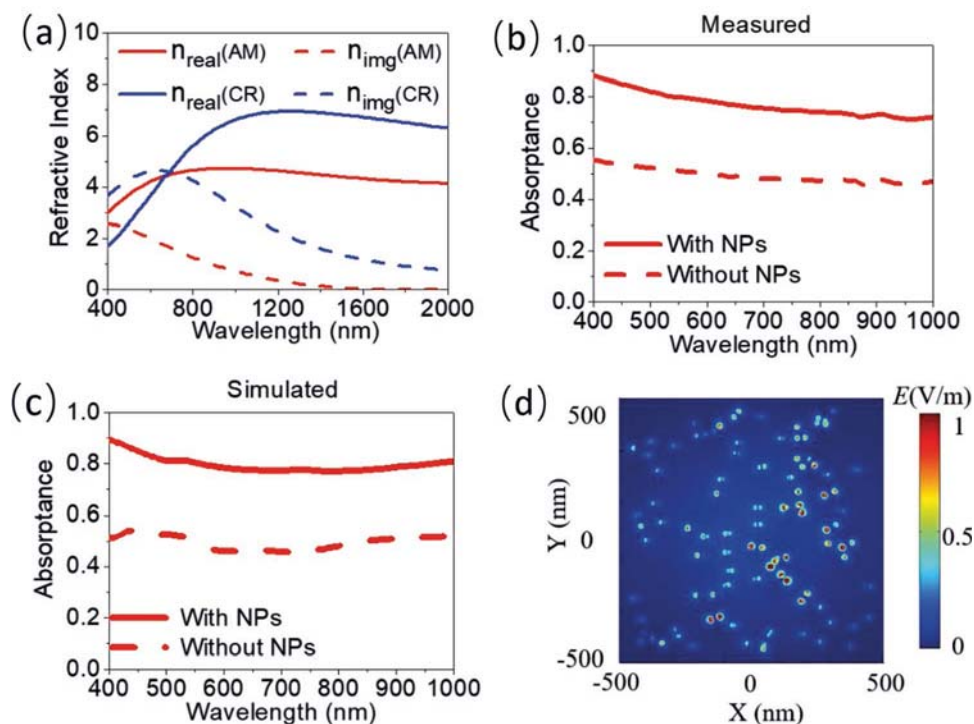


Figure 2. a) Complex refractive index of the GST film for both the amorphous (denoted as AM) and crystalline (denoted as CR) phases, where the complex refractive index was obtained using an ellipsometer to measure a 35 nm thick GST film on a silicon substrate. b) The measured and c) simulated absorbance for both the amorphous GST films coupled to Au NPs and the amorphous bare GST film, respectively. d) Total E -field distribution of the Au NPs coupled to the GST film at $\lambda = 563$ nm.

$\lambda = 563$ nm. In the simulation, the GST film thickness and Au NP diameter were measured from the SEM image shown in Figure 1b and defined as 35 and 50 nm, respectively. The dielectric constant of Au provided by Johnson & Christy was used.^[43] The permittivities of GST in the different structural states were extracted from the experimental data shown in Figure 2a. It is noteworthy that the roughness of the GST surface prevented a full contact between the Au NPs and GST film; therefore, a small separation between the particles and film was included in the model. The separation was adjusted to reduce the difference between the experimentally measured scattering spectra. A good agreement between the experiment and simulation was obtained for a gap of 3 nm. The resonant peak was attributed to the dipolar and quadrupolar hybridized mode, which is owing to the interference in the high refractive index GST film.^[44,45] The inset of Figure 1d shows the total E -field intensity distribution ($E = \sqrt{E_x^2 + E_y^2 + E_z^2}$) relative to the incoming total E -field at $\lambda = 563$ nm. As shown, the E -field is significantly enhanced near the air gap. The peak I_{scat} at $\lambda = 563$ nm corresponds to a strongly confined LSPR mode. At this wavelength, the peak E -field amplitude exceeded the incident E -field amplitude by a factor of 28. This was because the resonant peak originates from the interface mode, where the E -field was localized at the interface between the Au NP and GST film.^[23] Details of the numerical, fabrication, and measurement procedures are shown in Methods.

Figure 2a shows the measured complex dielectric permittivity spectrum of the GST film for both the amorphous (denoted as AM, red line) and crystalline (denoted as CR, blue line) states.

The complex refractive index of GST ($n = n_{\text{real}} + i \times n_{\text{img}}$) was measured using an infrared variable angle spectroscopic ellipsometer. The measurement was performed on a 35 nm thick GST film on a Si substrate. A Tauc–Lorentz model was selected for the fitting. The real part of the GST refractive index (n_{real} , solid line) was dispersive and the imaginary part was large (n_{img} , dashed line), implying a high absorption coefficient over the entire visible (vis) and near-infrared (NIR) regions. The reflectivity spectrum of the sample was measured using a QDI 2010 UV–visible–NIR range microspectrophotometer (CRAIC Technology Inc., San Dimas, CA).^[41] For this set of measurements, the incident light and collected light were at a normal incidence to the sample. The absorbance was then derived from $A(\omega) = 1 - T(\omega) - R(\omega)$. Because the structure does not transmit, this simplifies the absorbance to $A(\omega) = 1 - R(\omega)$. The $R(\omega)$ spectra were normalized to the Al reflector and determined as $R(\omega) = (R(\omega)_{\text{ns}} - R(\omega)_{\text{dark}}) / f(R(\omega)_{\text{Al}} - R(\omega)_{\text{dark}})$, where $R(\omega)_{\text{ns}}$ is the reflectance measured in the NPs coupled to the film, $R(\omega)_{\text{dark}}$ the reflectance of the structure when the white light source was off, $R(\omega)_{\text{Al}}$ the reflectance of a 100-nm-thick Al film deposited on a Si substrate, and $f(R(\omega)_{\text{Al}} - R(\omega)_{\text{dark}})$ the dark noise correction. Figure 2b shows the $A(\omega)$ for both the Au NPs coupled to the GST film (solid red line) and the bare GST film (dashed red line). In the GST-film-coupled Au NPs, a high absorbance of 80% was obtained over a broad spectral range from 400 to 1000 nm. A coalescence of the hybrid LSPR mode from the film-coupled NP system, which is shown in Figure 1d, was expected to couple to this broad absorbance of the GST layer.^[41,46,47] A bare GST layer possesses a significantly lower absorbance (50%) owing to

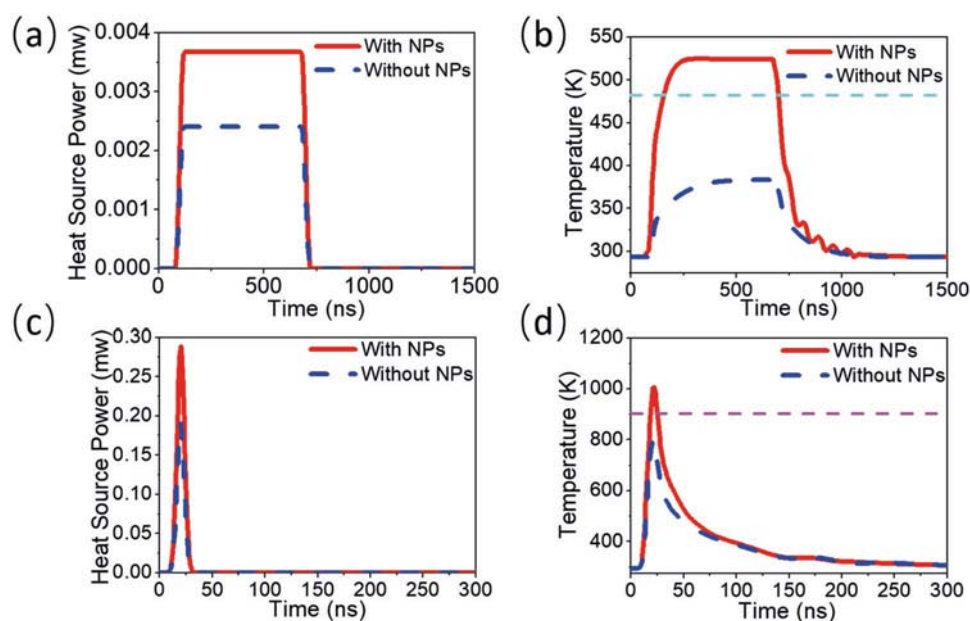


Figure 3. 3D finite element method (3D-FEM) simulations of a) heating power generated on the Au NPs coupled to the 35 nm thick amorphous GST film (solid red line), and a single 35 nm thick amorphous GST film (dashed blue line), b) time-dependent temperature distributions of the GST layers for both structures during crystallization, c) heat source powers, and d) time-dependent temperature distributions of the GST layers for the two structures during reamorphization.

the absence of the LSPR. This shows that dispersing Au NPs on the GST film can efficiently yield optical energy in the VIS–NIR spectrum. As shown in Figure 2c, we calculated the $A(\omega)$ spectra in both cases for an unpolarized normal illumination. The simulation validates the observed enhanced absorbance from the NPs coupled to the GST film. Figure 2d shows snapshots of the total E -field normalized to the incident E -field value at $\lambda = 563$ nm, where the E -fields are strongly localized around the Au NPs. Although the numerical simulations quantitatively show the key features of the measured enhanced spectra, differences are observed. In the simulations, the effects of surface roughness and fabrication imperfections were ignored. Moreover, the dispersed Au nanoparticles were considered perfect spheres in the theoretical model, which is impractical. We assumed that this simplification caused the observed differences between the measured and simulated absorbance spectra, as well as the differences in the I_{scat} spectra presented in Figure 1d.^[22,48–51] It is noteworthy that both the reflectance and I_{scat} spectra were measured in the far field over a finite acceptance angle within the microscope objective light cone. However, in the calculations, these spectra were calculated in the near field of the structures, which may have caused the differences between the experiments and simulations.

To experimentally illustrate the effect of Au NP size on the absorption spectra, we drop-cast NPs of different mean diameters, i.e., 30 (Figure S1a, Supporting Information), 50 (Figure S1b, Supporting Information), and 70 nm (Figure S1c, Supporting Information), onto the GST layer. As shown in Figure S1d (Supporting Information), the measured absorbance of the hybrid devices does not vary significantly with the diameter of the Au NPs.

The high absorbance in the film-coupled NPs allows a fast photothermal heating of the GST film. This results in a

rapid phase transition between the amorphous and crystalline states. The Set (crystallization) and Reset (reamorphization) operations of a GST cell occur at different temperatures and time scales. As shown in Figure 3, a heat transfer model was used to study temporal changes to the temperature of the GST dielectric layer for both the amorphous GST–Au NPs structure and a single amorphous layer without NPs. The COMSOL multiphysics modeling environment was employed to solve the coupled Fourier and Maxwell's equations numerically. The thermal conductivity of GST changes with temperature. The thermal characteristics of the materials used for the numerical model are summarized in Table S1 (Supporting Information).

The thermal energy absorbed by a unit cell is

$$I_{\text{th}}(r) = D^2 \times V \times I(r) \quad (1)$$

where r the distance from the center of the light beam, $D = 60$ nm the mean period of the Au NP array, $V = 0.80$ for the overlay integrals between the measured absorbance (Figure 2b) and the power density spectra of the light source, and $V = 0.53$ for the planar GST film. $I(r)$ represents the light fluence that illuminates the devices

$$I(r) = \frac{2I_0 e^{-\left(\frac{2r^2}{b^2}\right)}}{\pi b^2 F_r} \quad (2)$$

where I_0 is the power of the input Gaussian beams of 2 and 3.5 mW, b the beam waist of 1 and 10 μm , and F_r the repetition rate of 257 MHz and 25 kHz for the crystallization and reamorphization processing, respectively. The $I(r)$ for both the Set and Reset operations were determined by the excitation diode laser

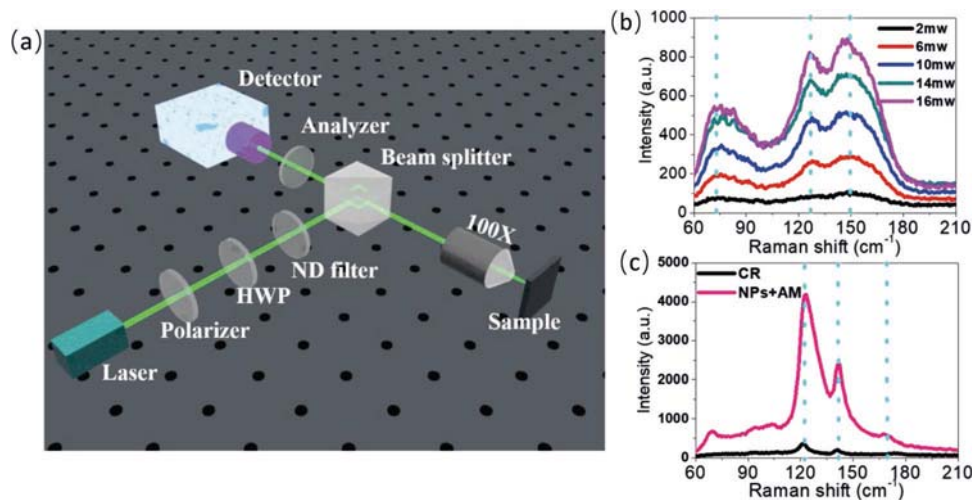


Figure 4. a) Experimental configuration for Raman spectroscopy. b) The measured Raman spectra of a 35 nm thick as-deposited amorphous GST film with the excitation powers of 2, 6, 10, 14, and 16 mW. c) Comparison of Raman signals from the Au NPs coupled to the amorphous (AM) GST film (pink solid line) and the bare crystalline (CR) GST film (solid black line) under the excitation power of 2 mW, where the thickness of the GST film was 35 nm.

in the Raman spectroscopy setup^[52] and the nanosecond pulse laser,^[53] respectively.

For the Set (crystallization) operation, the time-dependent laser heating source can be expressed by a square-wave waveform^[52]

$$M_s(r, t) = \begin{cases} I_{th}(r)E_r & t_0 \leq t \leq t_1 \\ 0 & t \leq t_0, t \geq t_1 \end{cases} \quad (3)$$

where $t_0 = 100$ ns and $t_1 = 700$ ns by assuming that the laser is operating for 600 ns.

For the Reset (reamorphization) operation, the nanosecond pulsed laser heating source is required^[53]

$$M_s(r, t) = I_{th}(r) \times \frac{1}{\sqrt{\pi\sigma}} e^{-\frac{(t-t_d)^2}{\sigma^2}} \quad (4)$$

where the time delay (t_d) and time constant (σ) of the pulsed lights were 20 and 5 ns for the reamorphization process, respectively.

Figure 3a shows the heat source power for both the GST-coupled NP structure and the GST film. The structures were placed at the beam focus. Figure 3b shows the temporal temperature distributions in the GST dielectric film for both structures. Our calculation shows that the temperatures within the as-deposited amorphous Au NP–GST structure increases with heating time and exceeds the amorphous-to-crystalline transition temperature of $T_C = 483$ K after ≈ 83 ns and a maximum temperature of 524 K after ≈ 163 ns for a threshold incident flux of 2.55 mW mm^{-2} . To fully crystallize GST, a subsequent annealing process was performed to maintain the GST temperature above $T_C = 483$ K but below $T_M = 873$ K for more than 50 ns.^[13] The temperature began decreasing to the room temperature (293K) after ≈ 325 ns once the heating source was turned off. This was caused by heat dissipation and radiation to the surrounding. Nevertheless, the bare GST film could not reach 483 K under the same excitation by the diode laser. A large temperature difference of 141 K between the two different

structures in Figure 3b was observed at 600 ns. The temperature distributions for both structures at 600 ns are presented in Figure S2a,b (Supporting Information). The figures show that the temperature within the GST layer covered by the Au NPs was significantly higher than that of the bare GST film, and the direction of the dominant temperature gradient points toward both the surrounding air and the Si substrate. To reset the GST cell into the amorphous state, the molten state must be quenched at a rate of 10^9 – 10^{10} K s^{-1} .^[54,55] Such a quench rate can be achieved using nanosecond pulsed lasers.^[2,17] As shown in Figure 3c, a 5 ns laser pulse with a power of 3.5 mW was applied to produce the heat source power for both the Au NP–GST coupled film and the bare GST film. Figure 3d shows the corresponding temporal temperature distributions in the GST film for both structures. For the Au NP–GST coupled structure, this laser pulse delivers sufficient energy to abruptly increase the temperature above T_M , which would melt GST. Subsequently, the GST melt can be quenched to the amorphous state by abruptly turning off the laser. We assumed melting as a prerequisite for amorphizing the GST film.

Our study indicates the usefulness of gap-mode plasmon resonances for reducing the switching power and time to heat GST to its crystallization and melting temperatures. The crystallization of amorphous GST film can be achieved with relatively low optical intensities within 600 ns. This matches the crystallization measurements for carefully thermally engineered structures.^[20] To prevent Au NPs from diffusing into the GST film after many cycles, SiO_2 or Si_3N_4 barrier layers of a few nanometers thick can be directly deposited between the Au NPs and GST film.^[53,56] Our proposed technique may be compatible with many types of GST alloys^[57] and wideband gap PCMs, such as Sb_2S_3 .^[58] This is because it does not require any complicated nanopatterning or device designs.

In addition to using gap-mode plasmons for reducing the optical power necessary to switch GST, **Figure 4** shows the measured Raman spectra for the Au NP–GST and bare GST structures. Raman scattering spectroscopy has been used to measure phonon modes and local structural motifs in GST.^[59]

In this study, we used Raman scattering spectroscopy to analyze the transition of GST from amorphous to crystalline. The samples must be exposed to the laser beam for ≈ 40 s to obtain a Raman signal. A schematic of the Raman spectroscopy setup is shown in Figure 4a. The Raman scattering spectra were collected and analyzed at room temperature using a spectrometer (Horiba iHR550). The structures were excited using a 532 nm solid state laser. The laser power was varied: 2, 6, 10, 14, and 16 mW. The spectra were recorded in the back-scattering geometry. The wavenumber resolution was ≈ 0.6 cm^{-1} . The laser source beam was focused using a $100 \times$ microscope with a 0.2 mm working distance. An air-cooled charge-coupled device (-70 °C) with a 1024×256 pixel front-illuminated chip was used to measure the scattering signal dispersed on a grating with 1800 grooves mm^{-1} . Figure 4b shows the Raman spectra of the as-deposited amorphous GST film of thickness 35 nm under the excitation powers of 2, 6, 10, 14, and 16 mW. The spectra of the amorphous GST film covered a broad band from 60–210 cm^{-1} and exhibits three central peaks at ≈ 73 , ≈ 127 , and ≈ 150 cm^{-1} , denoted as P_1 , P_2 , and P_3 , respectively. We attribute these peaks to the defective tetrahedral phonon modes.^[60]

The assignment of phonon modes was necessary to analyze the phase change from amorphous to crystalline. The Raman peak around ≈ 150 cm^{-1} (P_3) originates from the $A_{1g}(2)$ mode of Sb–Sb band vibrations in (Te_2) Sb–Sb(TeSb) or $(\text{Te}_2)\text{Sb}$ –Sb(Te_2), A_1 mode of GeTe_4 edge-sharing tetrahedra vibrations, and similar amorphous structures.^[61,62] The Raman band peaking at ≈ 127 cm^{-1} (P_2) was related to the $E_g(2)$ mode of Sb–Te band vibrations in the amorphous SbTe_3 pyramidal entities, and the A_1 mode of $\text{GeTe}_{4-n}\text{Ge}_n$ ($n = 1, 2$) corner- and/or edge-sharing tetrahedra according to the assignment in the amorphous GeTe film.^[63] The lowest Raman peak at ≈ 73 cm^{-1} (P_1) was attributed to the F_2 mode of the bending and antisymmetric stretching vibrations of GeTe_4 tetrahedra.^[61] As shown, the Raman signal intensity increased with the excitation power while maintaining the key spectral features. This indicates that the bare GST film was not crystallized with an incident laser power up to 16 mW, which was also indicated by the thermal model in Figure 3b.

To investigate the Raman spectra of the bare crystalline GST film, the as-deposited amorphous film was annealed on a hotplate for 30 min at 250 °C in a flowing argon atmosphere. In Figure 4c, the Raman spectra show that the crystallized GST film possesses at least three bands peaking at 122, 142, and 171 cm^{-1} , denoted as P_4 , P_5 , and P_6 , respectively, at a laser excitation power of 2 mW. Compared with the Raman spectra of the amorphous GST layer shown in Figure 4b, the Raman mode at ≈ 150 cm^{-1} (P_3) was not observed, indicating that the GST film was well crystallized.^[64] The peak at ≈ 150 cm^{-1} was caused by both the A_1 and $A_{1g}(2)$ modes. The $A_{1g}(2)$ mode, which is associated with Sb–Sb band vibrations, appeared in the hotplate-crystallized GST, while the A_1 mode corresponding to GeTe_4 edge-sharing tetrahedra vibrations was absent. The existing $A_{1g}(2)$ mode in the crystalline GST resulted in a Raman peak at 171 cm^{-1} (P_6).^[65,66] The Raman band peaking at 142 cm^{-1} (P_5) originates from the $A_1(\nu)$ mode of $\text{GeTe}_{4-n}\text{Ge}_n$ ($n = 1, 2$) corner-sharing tetrahedral.^[63] The Raman peak at 122 cm^{-1} (P_4) is related to the $E_g(2)$ mode of hexagonal Sb_2Te_3 .^[66] Figure 4c shows the measured Raman spectra of the GST film-coupled Au NPs under a minimum excitation laser power of 2 mW (solid pink line). It is interesting that at

only a 2 mW excitation power, the GST film covered by the Au NPs can be successfully crystallized. This is evident from the sharper Raman peaks, which have very similar energies to those of the hotplate-crystallized GST films (solid black line). In fact, the GST film coupled to Au NPs does not support a peak at 150 cm^{-1} , and its Raman peak locations are the same as those of the hotplate-crystallized GST sample. Based on the observation that the 16 mW excitation laser cannot crystallize the bare as-deposited amorphous GST film, see Figure 4b, it appears that the Au NPs increased the absorbed optical power, which is crucial. Moreover, the laser-crystallized Raman spectra exhibit peaks corresponding to GST of hexagonal (hex) crystal structure. Because hex-GST is formed at a higher temperature than the FCC phase, it appears the NP-GST coupled structure is heated extremely efficiently to a temperature substantially higher than necessary to form FCC GST.

More importantly, the Raman signal of the Au NPs coupled to the crystalline GST film increased by a factor of 12 over that of the bare crystalline GST film. The Au NPs concentrate the incident laser power, forming localized EM hot spots near the GST surface. Such gap-plasmon modes enhance the EM near field, which exists in a small volume around the GST–Au NPs interface. This effect is fundamentally the same as that responsible for surface-enhanced Raman amplification. Therefore, we expect new types of tunable SERS substrates, which we call GST-mediated SERS substrates, to be possible. Furthermore, the Au NPs may be replaced by Ag or Al NPs that are low in cost and compatible with CMOS technology.^[56] Clearly, diffusion barriers would be necessary.^[67]

3. Conclusion

We have experimentally and numerically demonstrated an approach to reduce the optical power necessary to crystallize GST phase-change films. This improvement was enabled without any complicated nanopatterning or thermal designs. The fabrication involved dispersing Au NPs onto the surface of a GST layer. Results indicated that coupling gap-mode plasmons to GST facilitated a low-power switching mode. Essentially, the gap-plasmon modes enhanced the EM field in a small volume of GST at the NP interface. Raman spectra from the structures indicated that the crystallization power could be reduced significantly using Au NPs. More importantly, a Raman enhancement factor of 12 under a pump wavelength of 532 nm was achieved. As the fabrication of Au NPs coupled to the GST film is a low-cost and fast process, we believe that this structure should be considered for the lower switchable photonics. Furthermore, we believe that this type of structure is applicable to switchable SERS substrates; therefore, it may be useful for noninvasive in situ analyses.

4. Experimental Section

Theoretical Model: For the numerical model, Lumerical Solutions, a commercial software that uses the FDTD method to solve Maxwell's equations, was used. In the simulation, the dispersive complex dielectric constant of GST was obtained from Figure 2a, and the dielectric

functions of Au were obtained from the literature.^[43] The geometry of the simulated Au NP was determined from its EBL image shown in Figure 1b. The computed domain was surrounded by perfectly matched layers to reduce reflections. A TM-polarized excitation source with an incident angle of 70° was used to calculate the scattering spectra and E-field distributions of the Au NPs coupled to the amorphous GST film. The illumination was modeled as a combination of the incident plane wave and the Fresnel waves reflected by the bare GST film. When calculating the field components scattered by the NPs, the field reflected from the GST film was ignored. A uniform 2 nm FDTD square mesh was used to reduce any numerical error when using the FDTD approach.

Sample Fabrications: A 35 nm thick GST film was deposited on a polished silicon (001) substrate using radio frequency sputtering (AJA Orion 5). The sputtering was performed in an Ar atmosphere at a pressure of 0.5 Pa. The chamber base pressure was better than 4×10^{-5} Pa. A colloidal solution of Au NPs of particle mean diameter 50 ± 2 nm was used. Au NPs were dropcast onto a GST layer and left to dry in air from an ethanol-diluted monodispersed Au NP colloidal solution (BB International). The substrate was heated to 60 °C to evaporate ethanol and avoid the aggregation of Au NPs.

Sample Measurements: White light was focused with a 100 × dark-field objective (OLYMPUS LMPLFLN-BD) using a lens of numerical aperture NA = 0.8. This provided a high-angle illumination and collection of scattering light. Individual nanoparticles on the GST film were characterized optically in a commercial microscope (Olympus BX53) using dark-field tungsten-light spectroscopy in reflection geometry. The precise positioning of a single nanoparticle was performed in confocal geometry using a set of selectable pixels with the imaging mode (Princeton Spectra Pro HRS-300) to limit the collection area on the sample. Dark-field spectra were recorded using a cooled spectrometer (Princeton Instruments PIX) at -70 °C and an integration time of 2 s. The scattering spectra of the Au NPs were achieved by collecting the scattered signal from the Au particle (I_p), deducting the scattered signal from a nearby area without a particle (I_r), and dividing by the latter, i.e., $I_{\text{scat}} = (I_p - I_r)/I_r$.

Supporting Information

Supporting Information is available from the Wiley Online Library or from the author.

Acknowledgements

This work was supported by Singapore-China Joint Research Program (JRP) with grant number 2015DFG12630 from the International Science & Technology Cooperation Program of China and an A*STAR AME Programmatic Grant A18A7b0058 (Singapore). T.C. acknowledges support from the Program for Liaoning Excellent Talents in University (Grant No. LJQ2015021). L.L. is grateful for his Ministry of Education President's Graduate Fellowship.

Conflict of Interest

The authors declare no conflict of interest.

Keywords

mid-infrared, phase-change materials, surface-enhanced Raman scattering, surface plasmon resonance, tunable

Received: September 17, 2019
Revised: December 3, 2019
Published online: January 13, 2020

- [1] M. Wuttig, *Nat. Mater.* **2005**, *4*, 265.
- [2] M. Wuttig, M. Salinga, *Nat. Mater.* **2012**, *11*, 270.
- [3] K. Shportko, S. Kremers, M. Woda, D. Lencer, J. Robertson, M. Wuttig, *Nat. Mater.* **2008**, *7*, 653.
- [4] M. Zhu, M. Xia, F. Rao, X. Li, L. Wu, X. Ji, S. Lv, Z. Song, S. Feng, H. Sun, *Nat. Commun.* **2014**, *5*, 4086.
- [5] J. Rice, *Micron Announces Availability of Phase Change Memory for Mobile Devices*, Micron Technologies Inc., Boise, Idaho **2012**, <https://www.micron.com>.
- [6] L. Hoddeson, P. K. Garrett, *Phys. Today* **2018**, *71*, 44.
- [7] R. Simpson, M. Krbal, P. Fons, A. Kolobov, J. Tominaga, T. Uruga, H. Tanida, *Nano Lett.* **2010**, *10*, 414.
- [8] M. H. Lankhorst, B. W. Ketelaars, R. A. Wolters, *Nat. Mater.* **2005**, *4*, 347.
- [9] H. F. Hamann, M. O'Boyle, Y. C. Martin, M. Rooks, H. K. Wickramasinghe, *Nat. Mater.* **2006**, *5*, 383.
- [10] W. Wełnic, M. Wuttig, *Mater. Today* **2008**, *11*, 20.
- [11] D. Lencer, M. Salinga, B. Grabowski, T. Hickel, J. Neugebauer, M. Wuttig, *Nat. Mater.* **2008**, *7*, 972.
- [12] H. Peng, K. Cil, A. Gokirmak, G. Bakan, Y. Zhu, C. Lai, C. Lam, H. Silva, *Thin Solid Films* **2012**, *520*, 2976.
- [13] N. Yamada, E. Ohno, N. Akahira, K. i. Nishiuchi, K. i. Nagata, M. Takao, *Jpn. J. Appl. Phys.* **1987**, *26*, 61.
- [14] J. Orava, A. á. Greer, B. Gholipour, D. Hewak, C. Smith, *Nat. Mater.* **2012**, *11*, 279.
- [15] H. Zhu, J. Yin, Y. Xia, Z. Liu, *Appl. Phys. Lett.* **2010**, *97*, 083504.
- [16] S. Selmo, R. Cecchini, S. Cecchi, C. Wiemer, M. Fanciulli, E. Rotunno, L. Lazzarini, M. Rigato, D. Pogany, A. Lugstein, *Appl. Phys. Lett.* **2016**, *109*, 213103.
- [17] J. K. Behera, X. Zhou, J. Tominaga, R. E. Simpson, *Opt. Mater. Express* **2017**, *7*, 3741.
- [18] P. K. Khulbe, E. M. Wright, M. Mansuripur, *J. Appl. Phys.* **2000**, *88*, 3926.
- [19] T. Cao, C. Wei, R. E. Simpson, L. Zhang, M. J. Cryan, *Opt. Mater. Express* **2013**, *3*, 1101.
- [20] M. Wuttig, H. Bhaskaran, T. Taubner, *Nat. Photonics* **2017**, *11*, 465.
- [21] T. Cao, C.-. Wei, R. E. Simpson, L. Zhang, M. J. Cryan, *Sci. Rep.* **2015**, *4*, 3955.
- [22] C. Lumdee, B. Yun, P. G. Kik, *ACS Photonics* **2014**, *1*, 1224.
- [23] T. Hira, T. Homma, T. Uchiyama, K. Kuwamura, T. Saiki, *Appl. Phys. Lett.* **2013**, *103*, 241101.
- [24] J. A. Schuller, E. S. Barnard, W. Cai, Y. C. Jun, J. S. White, M. L. Brongersma, *Nat. Mater.* **2010**, *9*, 193.
- [25] P. Biagioni, J.-S. Huang, B. Hecht, *Rep. Prog. Phys.* **2012**, *75*, 024402.
- [26] S. A. Maier, *IEEE J. Sel. Top. Quantum Electron.* **2006**, *12*, 1671.
- [27] S. Kawata, Y. Inouye, P. Verma, *Nat. Photonics* **2009**, *3*, 388.
- [28] J. N. Anker, W. P. Hall, O. Lyandres, N. C. Shah, J. Zhao, R. P. Van Duyne, in *Nanoscience and Technology: A Collection of Reviews from Nature Journals* (Ed: P. Rodgers), World Scientific, Singapore **2010**, pp. 308–319.
- [29] R. T. Hill, J. J. Mock, Y. Urzhumov, D. S. Sebba, S. J. Oldenburg, S.-Y. Chen, A. A. Lazarides, A. Chilkoti, D. R. Smith, *Nano Lett.* **2010**, *10*, 4150.
- [30] S.-Y. Chen, J. J. Mock, R. T. Hill, A. Chilkoti, D. R. Smith, A. A. Lazarides, *ACS Nano* **2010**, *4*, 6535.
- [31] S. Mubeen, S. Zhang, N. Kim, S. Lee, S. Krämer, H. Xu, M. Moskovits, *Nano Lett.* **2012**, *12*, 2088.
- [32] Z. M. Jin, W. Gu, X. B. Shi, Z. K. Wang, Z. Q. Jiang, L. S. Liao, *Adv. Opt. Mater.* **2014**, *2*, 588.
- [33] V. Merk, J. Kneipp, K. Leosson, *Adv. Opt. Mater.* **2013**, *1*, 313.
- [34] A. B. Vasista, S. K. Chaubey, D. J. Gosztoła, G. P. Wiederrecht, S. K. Gray, G. P. Kumar, *Adv. Opt. Mater.* **2019**, *7*, 1900304.
- [35] A. Tittl, X. Yin, H. Giessen, X.-D. Tian, Z.-Q. Tian, C. Kremers, D. N. Chigrin, N. Liu, *Nano Lett.* **2013**, *13*, 1816.
- [36] L. R. Hirsch, R. J. Stafford, J. Bankson, S. R. Sershen, B. Rivera, R. Price, J. D. Hazle, N. J. Halas, J. L. West, *Proc. Natl. Acad. Sci. USA* **2003**, *100*, 13549.

- [37] X. Huang, I. H. El-Sayed, W. Qian, M. A. El-Sayed, *J. Am. Chem. Soc.* **2006**, *128*, 2115.
- [38] B. del Rosal, A. Pérez-Delgado, E. Carrasco, D. J. Jovanović, M. D. Dramićanin, G. Dražić, Á. J. de la Fuente, F. Sanz-Rodríguez, D. Jaque, *Adv. Opt. Mater.* **2016**, *4*, 782.
- [39] C. Lumdee, S. Toroghi, P. G. Kik, *ACS Nano* **2012**, *6*, 6301.
- [40] C. Lumdee, B. Yun, P. G. Kik, *J. Phys. Chem. C* **2013**, *117*, 19127.
- [41] J. C. Dong, R. Panneerselvam, Y. Lin, X. D. Tian, J. F. Li, *Adv. Opt. Mater.* **2016**, *4*, 1144.
- [42] D. Y. Lei, A. I. Fernández-Domínguez, Y. Sonnefraud, K. Appavoo, R. F. Haglund Jr., J. B. Pendry, S. A. Maier, *ACS Nano* **2012**, *6*, 1380.
- [43] P. B. Johnson, R.-W. Christy, *Phys. Rev. B* **1972**, *6*, 4370.
- [44] S. Zhang, K. Bao, N. J. Halas, H. Xu, P. Nordlander, *Nano Lett.* **2011**, *11*, 1657.
- [45] I. Tanabe, T. Tsuma, *Nano Lett.* **2012**, *12*, 5418.
- [46] Y. Avitzour, Y. A. Urzhumov, G. Shvets, *Phys. Rev. B* **2009**, *79*, 045131.
- [47] J. Wang, C. Fan, P. Ding, J. He, Y. Cheng, W. Hu, G. Cai, E. Liang, Q. Xue, *Opt. Express* **2012**, *20*, 14871.
- [48] V. Myroshnychenko, J. Rodríguez-Fernández, I. Pastoriza-Santos, A. M. Funston, C. Novo, P. Mulvaney, L. M. Liz-Marzán, F. J. G. de Abajo, *Chem. Soc. Rev.* **2008**, *37*, 1792.
- [49] Y. H. Fu, A. I. Kuznetsov, A. E. Miroshnichenko, Y. F. Yu, B. Luk'yanchuk, *Nat. Commun.* **2013**, *4*, 1527.
- [50] M. Yorulmaz, S. Nizzero, A. Hoggard, L.-Y. Wang, Y.-Y. Cai, M.-N. Su, W.-S. Chang, S. Link, *Nano Lett.* **2015**, *15*, 3041.
- [51] A. Tcherniak, J. Ha, S. Dominguez-Medina, L. Slaughter, S. Link, *Nano Lett.* **2010**, *10*, 1398.
- [52] H. H. Richardson, M. T. Carlson, P. J. Tandler, P. Hernandez, A. O. Govorov, *Nano Lett.* **2009**, *9*, 1139.
- [53] B. Gholipour, J. Zhang, K. F. MacDonald, D. W. Hewak, N. I. Zheludev, *Adv. Mater.* **2013**, *25*, 3050.
- [54] N. Yamada, E. Ohno, K. Nishiuchi, N. Akahira, M. Takao, *J. Appl. Phys.* **1991**, *69*, 2849.
- [55] V. Weidenhof, N. Pirch, I. Friedrich, S. Ziegler, M. Wuttig, *J. Appl. Phys.* **2000**, *88*, 657.
- [56] W. Dong, Y. Qiu, J. Yang, R. E. Simpson, T. Cao, *J. Phys. Chem. C* **2016**, *120*, 12713.
- [57] M. Behrens, A. Lotnyk, J. W. Gerlach, M. Ehrhardt, P. Lorenz, B. Rauschenbach, *ACS Appl. Mater. Interfaces* **2019**, *11*, 41544.
- [58] W. Dong, H. Liu, J. K. Behera, L. Lu, R. J. Ng, K. V. Sreekanth, X. Zhou, J. K. Yang, R. E. Simpson, *Adv. Funct. Mater.* **2019**, *29*, 1806181.
- [59] D. Lencer, M. Salinga, M. Wuttig, *Adv. Mater.* **2011**, *23*, 2030.
- [60] G. C. Sosso, S. Caravati, R. Mazzarello, M. Bernasconi, *Phys. Rev. B* **2011**, *83*, 134201.
- [61] L. Petit, N. Carlie, F. Adamietz, M. Couzi, V. Rodriguez, K. Richardson, *Mater. Chem. Phys.* **2006**, *97*, 64.
- [62] S. Guo, Z. Hu, X. Ji, T. Huang, X. Zhang, L. Wu, Z. Song, J. Chu, *RSC Adv.* **2014**, *4*, 57218.
- [63] K. Andrikopoulos, S. Yannopoulos, G. Voyiatzis, A. Kolobov, M. Ribes, J. Tominaga, *J. Phys.: Condens. Matter* **2006**, *18*, 965.
- [64] H. Yoon, W. Jo, E. Cho, S. Yoon, M. Kim, *J. Non-Cryst. Solids* **2006**, *352*, 3757.
- [65] W. Richter, C. Becker, *Phys. Status Solidi B* **1977**, *84*, 619.
- [66] G. Sosso, S. Caravati, M. Bernasconi, *J. Phys.: Condens. Matter* **2009**, *21*, 095410.
- [67] L. Lu, W. Dong, J. K. Behera, L. Chew, R. E. Simpson, *J. Mater. Sci.* **2019**, *54*, 2814.